JGR Solid Earth

RESEARCH ARTICLE
10.1029/2021JB022741

Key Points:

- New iterative stacking scheme based on Historical Interstation Pattern Referencing improves the data quality assessment for deep Earth studies
- Refined waveform stacks more objectively and systematically incorporate station and event quality, providing interpretation confidence
- Application to PcP phases recorded by an Antarctic seismic array provides evidence for ultra-low velocity zone structure east of New Zealand

Supporting Information:

Supporting Information may be found in the online version of this article.

Correspondence to:

S. E. Hansen,
shansen@geo.ua.edu

Citation:

Hansen, S. E., Garnero, E. J., & Rost, S. (2021). Historical Interstation Pattern Referencing (HIPR): An application to PcP waves recorded in the Antarctic for ULVZ imaging. *Journal of Geophysical Research: Solid Earth*, *126*, e2021JB022741. https://doi.org/10.1029/2021JB022741

Received 1 JUL 2021
Accepted 10 OCT 2021

Historical Interstation Pattern Referencing (HIPR): An Application to PcP Waves Recorded in the Antarctic for ULVZ Imaging

Samantha E. Hansen[1], Edward J. Garnero[2], and Sebastian Rost[3]

[1]The University of Alabama, Tuscaloosa, AL, USA, [2]Arizona State University, Tempe, AZ, USA, [3]The University of Leeds, Leeds, UK

Abstract Much of our knowledge on deep Earth structure is based on detailed analyses of seismic waveforms that often have small amplitude arrivals on seismograms; therefore, stacking is essential to obtain reliable signals above the noise level. We present a new iterative stacking scheme that incorporates Historical Interstation Pattern Referencing (HIPR) to improve data quality assessment. HIPR involves comparing travel-time and data quality measurements between every station for every recorded event to establish historical patterns, which are then compared to individual measurements. Weights are determined based on the individual interstation measurement differences and their similarity to historical averages, and these weights are then used in our stacking algorithm. This approach not only refines the stacks made from high-quality data but also allows some lower-quality events that may have been dismissed with more traditional stacking approaches to contribute to our study. Our HIPR-based stacking routine is illustrated through an application to core-reflected PcP phases recorded by the Transantarctic Mountains Northern Network to investigate ultra-low velocity zones (ULVZs). We focus on ULVZ structure to the east of New Zealand because this region is well-sampled by our data set and also coincides with the boundary of the Pacific Large Low Shear Velocity Province (LLSVP), thereby allowing us to further assess possible ULVZ-LLSVP relationships. The HIPR-refined stacks display strong ULVZ evidence, and associated synthetic modeling suggests that the ULVZs in this region are likely associated with compositionally distinct material that has perhaps been swept by mantle convection currents to accumulate along the LLSVP boundary.

Plain Language Summary Our understanding of deep Earth structure is largely based on studies that use small amplitude, earthquake-generated signals that have interacted with structures near the Earth's core-mantle boundary (CMB). Multiple seismic records are typically averaged (stacked) to improve the signal-to-noise ratio of these signals; however, the stacked signals can still be challenging to interpret if they are based on low quality data. Here, we develop a new iterative stacking approach that compares travel-time and data quality measurements between all stations and all recorded events to develop historical patterns, which are then compared to individual measurements. Event and station weights based on the interstation measurement differences and their similarity to historical averages are used in our stacking algorithm to refine the signals of interest, thereby providing further confidence in events chosen for modeling and interpretation. Our approach is applied to seismic waves that have been reflected from the Earth's core and recorded by an Antarctic deployment, allowing us to explore the lowermost mantle structure east of New Zealand. Our results show strong evidence for anomalous CMB structure, which may be associated with chemically distinct material that has accumulated in the region due to mantle convection currents.

1. Introduction

The core-mantle boundary (CMB), where the solid silicate mantle meets the predominantly iron fluid outer core, represents the largest absolute density contrast within the Earth. It has long been recognized that the lowermost mantle and the CMB display significant structural complexities, on the order of those seen within the crust, and these complexities likely play a critical role in the thermal and chemical evolution of our planet (e.g., Garnero, 2000; Hernlund & Bonati, 2019; Liu et al., 2016; Williams & Garnero, 1996). However, investigating lower mantle and CMB heterogeneities is challenging. Studies often rely on small-amplitude

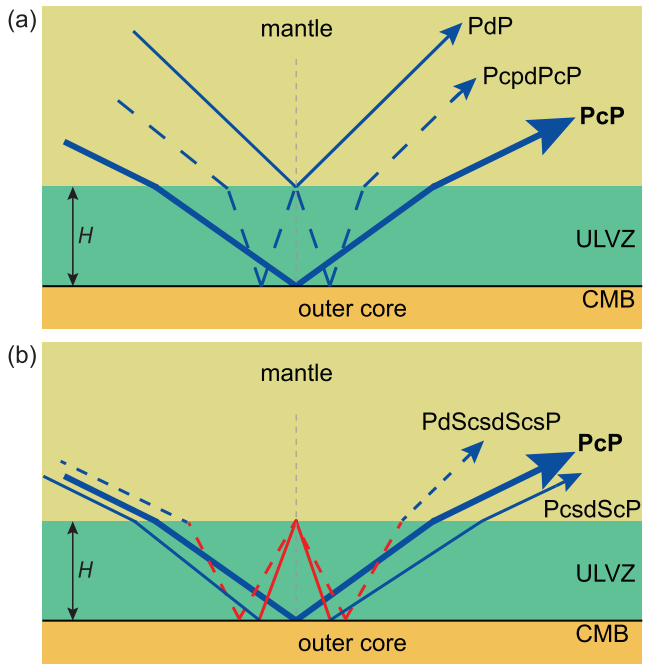

Figure 1. Cartoons illustrating PcP interaction with a ultra-low velocity zone (ULVZ; modified from Yu & Garnero, 2018). Blue ray paths are P-waves, red ray paths are S-waves, and *H* indicates ULVZ thickness. (a) Pre- (PdP) and post-cursors (PcpdPcP) resulting from reflections along the top and from the underside of the mantle-ULVZ boundary. In this panel, all seismic phase legs are P-waves. (b) Additional underside reflections from the mantle-ULVZ boundary that have two (PcsdScP) or four (PdScsdScsP) S-wave legs. Panel separation and line style (solid or dashed) is just provided for clarity.

reflected or long-path diffracted seismic phases that may have non-uniform and/or sparse coverage (e.g., Lai & Garnero, 2019) and which can be difficult to interpret, especially if the corresponding signal-to-noise ratio (SNR) is low. Further, non-ideal array locations can also complicate studies of deep Earth structure. For example, if seismically slow layers, such as ice sheets or thick sediment deposits, are present at the surface, reverberant energy from within these layers can lower the SNR of recorded data. Therefore, approaches that allow for improved imaging are important for the development of confident interpretations of lowermost mantle and CMB structural variabilities.

In this study, we develop a unique approach to improve the quality of stacked seismic data and to provide robust sampling of small-scale, deep Earth heterogeneities. Event and station weights based on Historical Interstation Pattern Referencing (HIPR) are computed using travel-times, SNR values, and waveform similarities. The weights are then incorporated into an iterative stacking routine, and the resulting waveforms are modeled by comparing the observed signals with predicted synthetic waveforms. Our HIPR-weighted stacking method not only refines the signals for high SNR data but also allows some lower-quality events that may have been dismissed with more traditional stacking approaches to contribute to our investigation.

1.1. Applying the New Stacking Approach

To illustrate our approach, the method is applied to core-reflected PcP waves (Figure 1) recorded by the Transantarctic Mountains Northern Network (TAMNNET), a 15-broadband-station seismic array that was deployed in Antarctica from 2012 to 2015 (Figure 2a; Hansen et al., 2015). This data set allows for a range of assessment opportunities. PcP waves are commonly employed to investigate ultra-low velocity zones (ULVZs) along the CMB (e.g., Gassner et al., 2015; Hutko et al., 2009; Kohler et al., 1997; Mori & Helmberger, 1995; Persh & Vidale, 2004; Revenaugh & Meyer, 1997; Rost et al., 2010). ULVZs are small-scale (5–50 km thick), laterally varying structures that have been detected in some locations just above the CMB, and they are typically characterized by P-wave velocity reductions (δV_P) up to ~20%, S-wave velocity reductions (δV_S) up to ~50%, and density perturbations ($\delta\rho$) up to ~20% (Yu & Garnero, 2018 and references therein). The lateral extent of ULVZs is generally reported as being ~100–200 km, though in some cases, ULVZs up to ~1,000 km wide have been reported (e.g., Cottaar & Romanowicz, 2012; Jenkins et al., 2021; Thorne et al., 2013; Zhao et al., 2017). The source of ULVZs is still widely debated, but some studies attribute them to thermal anomalies, possibly associated with partial melt, along the CMB (Garnero & Vidale, 1999; Reasoner & Revenaugh, 2000; Rost et al., 2006; Williams & Garnero, 1996). It has also been suggested that the locations of ULVZs correlate with hotspots and that ULVZs may feed mantle plumes (Cottaar & Romanowicz, 2012; Garnero, 2000; Williams et al., 1998). However, some ULVZs have been identified outside warm portions of the lower mantle, and in these cases, ULVZs are typically attributed to compositional anomalies along the CMB. Such heterogeneities may be associated with iron-enriched material created by chemical reactions between the mantle and the core (Knittle & Jeanloz, 1991; Li et al., 2016; Mao et al., 2006; Wicks et al., 2010) or with remnants of subducted material (Andrault et al., 2014; Dobson & Brodholt, 2005; Hirose et al., 1999, 2005; Liu et al., 2016).

When PcP phases encounter a ULVZ, both pre- and post-cursor signals can be generated from reflections off the top and from the underside of the structural discontinuity, respectively (Figure 1). Modeling waveforms for these pre- and post-cursors allows ULVZ structure to be characterized, thereby permitting assessment of potential origin mechanisms. That said, PcP can be a difficult seismic phase to identify and interpret. PcP waves inherently have fairly low amplitudes since a significant portion of the energy continues into the core as a PKP wave, reducing the P-to-P reflection coefficient at the CMB. This is very different from transverse

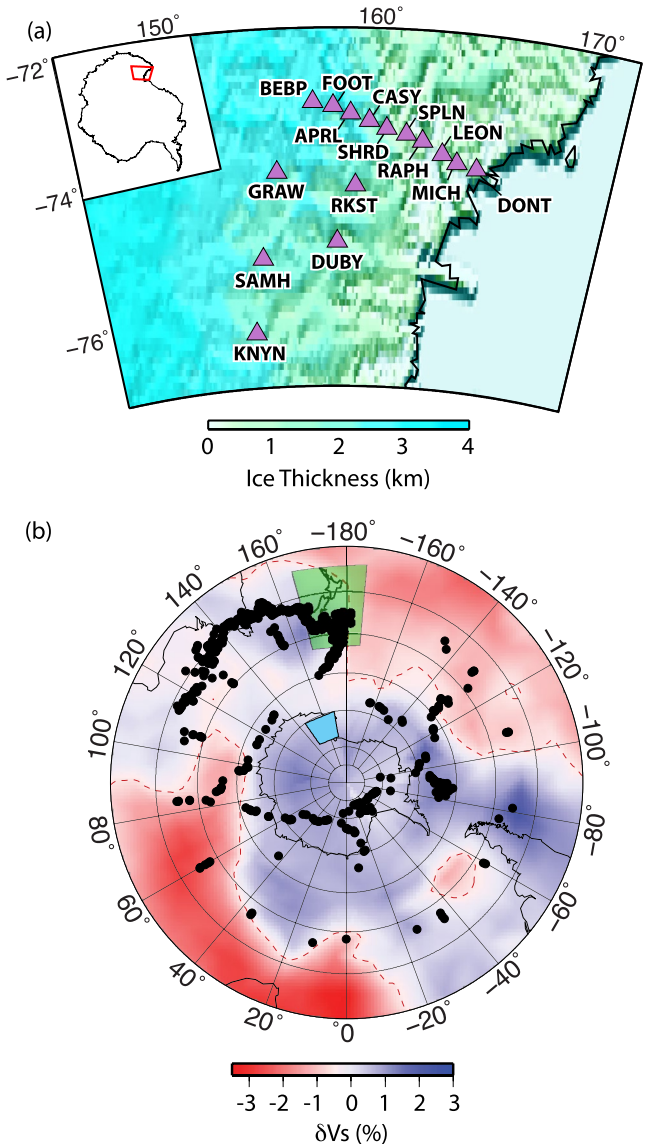

Figure 2. (a) Map showing TAMNNET stations (purple triangles), overlain on ice thickness estimates from BEDMAP2 (Fretwell et al., 2013). Station names are also listed. The location of this map in relation to the rest of the Antarctic continent is shown by the red polygon on the inset (upper left). (b) Map of average PcP CMB bounce points (black dots) for the 822 events in our base data set. The GyPSuM tomography model (Simmons et al., 2010) at 2,800 km depth is shown in the background, with red dashed lines highlighting the LLSVP boundaries. Cyan polygon marks the location of the TAMNNET array shown in panel (a), and green polygon denotes the area near New Zealand, which is the focus of our example application in Section 6.

component ScS waves, in which 100% of the energy reflects from the CMB. Scattered energy in the direct P-wave coda and other noise can also reduce the PcP SNR. While stacking methodologies help to improve PcP signals, the small amplitude of this phase can still be difficult to distinguish if the stacks are based on low quality waveforms. We will use the TAMNNET PcP data set to demonstrate that our approach generates robust, weighted stacks that can be reliably interpreted for ULVZ structure.

The location of the TAMNNET array also contributes to the uniqueness of our data set. Like many networks in Antarctica, TAMNNET was deployed to investigate the crustal and upper mantle characteristics of this largely unconstrained continent (Hansen et al., 2015). All TAMNNET stations were deployed on the East Antarctic Ice Sheet (Figure 2a), and this slow-velocity near-surface layer is a source of reverberant energy. Sampling of the lowermost mantle and CMB structure beneath the polar regions is sparse (e.g., Hansen et al., 2020; Yu & Garnero, 2018), and to expand coverage of the CMB in these regions, non-ideal data sets like TAMNNET need to be employed. While a suite of PcP data is incorporated into our refined stacking approach, we focus our interpretations on imaged ULVZ structure in the vicinity of New Zealand since this region is particularly well-populated with events that occurred during the TAMNNET deployment. Further, the area is well suited to test the HIPR approach because prior studies (Hansen et al., 2020; Thorne & Garnero, 2004; Thorne et al., 2020) have reported varied ULVZ evidence near New Zealand, and the region borders the Pacific Large Low Shear Velocity Province (LLSVP), which may influence ULVZs (see Section 6). Our results not only help to expand lowermost mantle constraints along this portion of the CMB, but they also illustrate the usefulness of the HIPR method when modeling sometimes poor-quality seismic phases recorded by arrays which were deployed in complex environments and that have not necessarily been designed for deep Earth investigations.

2. Data Selection, Pre-Processing, and Initial Stacking Procedure

To investigate PcP in this study, the TAMNNET-recorded earthquakes were limited to event-station distances between 30° and 75° and to magnitudes ≥5.0. PcP phases in this distance range typically have favorable reflection coefficients from the CMB (e.g., Rost et al., 2010), and the SNR of PcP waves from smaller magnitude (<5.0) earthquakes is generally too low to reliably interpret the signal. These selection criteria yielded a total of 2,274 events. For each earthquake, several pre-processing steps were required. Specifically, the vertical and radial component waveforms were rotated to true longitudinal motion directions for P and PcP arrivals using their corresponding incidence angles, as predicted by the Preliminary Reference Earth Model (PREM; Dziewonski & Anderson, 1981). Comparable to other PcP investigations (e.g., Gassner et al., 2015; Persh & Vidale, 2004; Rost et al., 2010), all data were bandpass-filtered between 0.50 and 1.50 Hz (two poles), and PREM-predicted P and PcP arrival times were determined and marked on all seismograms. The rotated and filtered data were visually inspected for any evidence of identifiable PcP energy and were retained if present. This reduced our data set to 822 events, and these events form the base for our analyses (Figure 2b).

For each event, our first processing step was to create initial stacks from the individual waveforms across all stations (Figure 3). These stacks were generated for the P phase first, followed by a separately generated

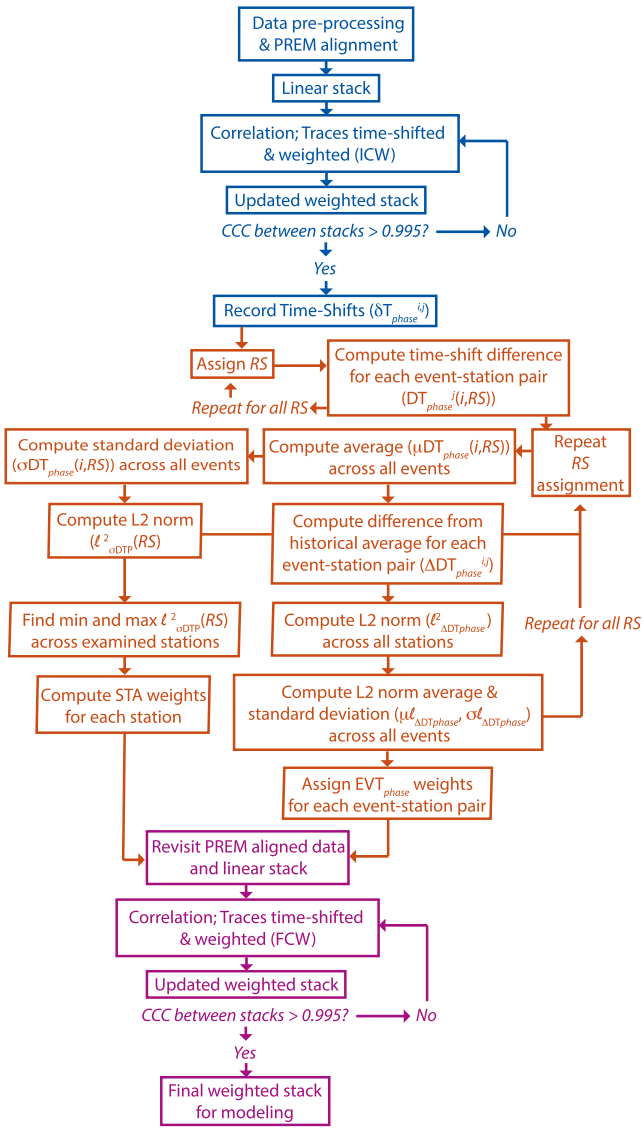

Figure 3. Flowchart outlining the main processing steps of the new Historical Interstation Pattern Referencing methodology. The portion of the flowchart in blue corresponds to Section 2 in the text, orange corresponds to Section 3, and purple corresponds to Section 4.

stack for the PcP phase. The P waveforms were initially aligned using the PREM-predicted arrival times, with the data windowed ±25 s around the theoretical P arrival time. Their maximum amplitudes were normalized to unity, and the data were then averaged to create a linear stack. Each individual P waveform was then cross-correlated with the linear stack (over a 10 s window around P) to compute a delay time and a cross-correlation coefficient (CCC), somewhat similar to the approach developed by Rawlinson and Kennett (2004). The delay times were used to shift the individual waveforms in order to improve the alignment of the P phases, and the square of the CCC (CCC^2) was retained as a weighting factor for each waveform. A second weighting factor (SNR_{weight}) was also developed, based on the SNR of the individual P waveforms, where the signal was defined by a window extending 5 s before and 10 s after P, and the noise was defined by a 15 s window situated 10 s ahead of P. If the P-wave SNR ≥10, the SNR_{weight} is set to a full weight of 1; if the P-wave SNR is ≤1, the waveform is given an SNR_{weight} of 0.05; and if the SNR falls in between these end-member values, the SNR_{weight} is determined with a linear ramp function. The product of these two weights defines an initial composite weight ($ICW = CCC^2 \times SNR_{weight}$) that is applied to each waveform. We also note that the time shifts for individual waveforms were limited to ±4 s because an examination of the arrivals across the TAMNNET array indicated that it would be unlikely for an individual station to have more than a 4 s time shift relative to its peers. If a given waveform had a larger time shift, its corresponding weight was set to 0, essentially removing it from the data set. The realigned and weighted waveforms were then restacked. Using the updated stack, new waveform weights were determined, and the stacking process was iteratively repeated until the CCC between the current and previous stack exceeded 0.995. This approach optimizes the alignment of the individual waveforms and creates a representative P stack for each event. On average, two iterations were required to create an optimal stack.

For the PcP waveforms, the initial stacking procedure is very similar; however, since P phases have higher SNRs than PcP, it was determined that if the P signal is unclear, then the lower amplitude PcP arrival is likely unreliable. Therefore, after the individual PcP waveforms were aligned on their PREM-predicted arrival times, they were adjusted using the total correlation-based time shift determined for their corresponding P waveform. Also, if the corresponding P waveform was given a weight of 0 during the iterative stacking routine described above, the PcP waveform was also assigned a weight of 0. Further, the individual PcP waveforms were examined for potentially interfering depth phases (pP, sP, PP, and associated reflections/triplications), and in cases where such depth phases interfered with the PcP arrival, the individual waveform was removed from consideration. The PcP waveforms were then averaged to create a linear stack, and that stack was cross-correlated with each individual PcP record (again, over a 10 s window around PcP). As with the P phases, the PcP waveforms were weighted by the product of a correlation weight (CCC^2) and an SNR_{weight}. For this phase, the end-member SNR values were 2 and 0.5, corresponding to SNR_{weight} values of 1 and 0.05, respectively, with a linear ramp function again used to determine the SNR_{weight} for intermediate SNR values. The same iterative stacking procedure as described for the P data was applied to the realigned, weighted PcP waveforms, again to optimize the waveform alignment and to create a representative stack. Typically, about four iterations were required for the PcP stack to converge given the lower SNR of this phase compared to the P-waves. Figure 4 shows example P and PcP waveforms before and after re-alignment, along with the initial and final stacks for both phases. For all events and all stations, the correlation-based time shifts for both the P and PcP waveforms were recorded (Figure 3).

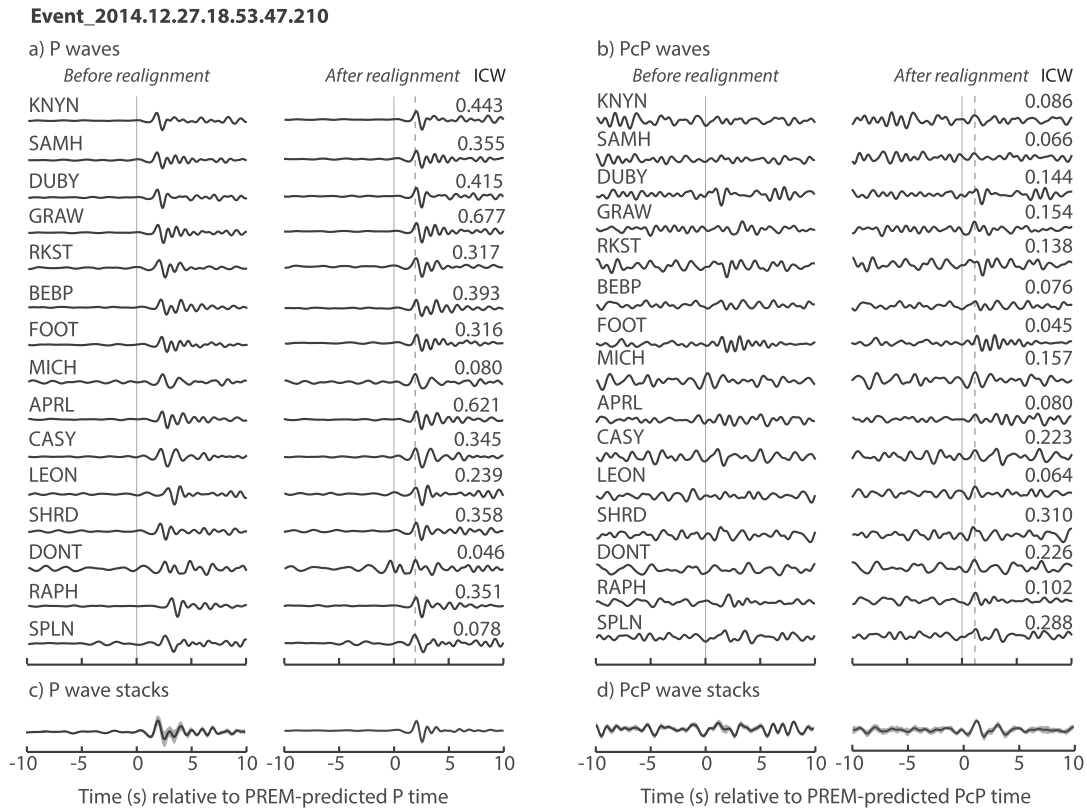

Figure 4. Examples of initial P and PcP alignment and stacking. Waveforms correspond to an event that occurred on December 27, 2014 recorded by TAMNNET. The normalized (a) P- and (b) PcP-waves are originally aligned on their PREM-predicted arrival times (Dziewonski & Anderson, 1981), which are marked by the thin gray lines on the "*Before realignment*" panels. Using the initial stacking procedure outlined in Section 2, the waveforms are realigned on the waveform peak, as shown in the "*After realignment*" panels, where the dashed gray lines mark the peaks of the arrivals. Station names are listed on the left, and initial composite weights (ICW) are listed on the right. We note that these weights are comparable to those determined for other TAMNNET-recorded events. The corresponding (c) P and (d) PcP stacks, both before and after realignment, are also shown with one standard deviation indicated by the gray shading.

All 822 events in the base data set were processed using the approach outlined above. The corresponding stacks were then visually examined to identify those with clear P and PcP arrivals to create a subset of high-quality events for the interstation analysis described in the next section. The selected events had P stacks with an average SNR of 36.5 and an average CCC of 0.87, while the selected PcP stacks had an average SNR and CCC of 2.7 and 0.74, respectively. In total, 227 events were retained. Generally, the selected events were deeper (average depth of ~166 km) compared to the remaining events (average depth of ~54 km), which may partially explain their higher SNR and CCC values.

3. HIPR Weighting Approach

As outlined in the previous section, the P and PcP waveforms were iteratively time-shifted to create optimized, weighted stacks. For a given station, the applied time shift used for the final stack may vary significantly from one event to another. This could be caused by source mislocation, structural heterogeneity between the earthquake and the receiver, and/or small-scale structures beneath the array; therefore, it is generally not possible to determine the cause(s) of individual record absolute time-shift values. However, this uncertainty is significant because it is important to assess whether a particular pre-stack time shift may be erroneous. An example of this would be the alignment of noise events in the waveforms rather than the signals of interest.

By examining the time-shift differences between stations, especially across a large number of events, we can gain a better understanding of which timing variations are similar to historical averages versus those that

depart from typical values. In other words, the stability of the time-shift measurements at each station in the array can be systematically evaluated. Ultimately, this approach not only quantifies high- versus low-quality data, but it also allows us to define weights for each event and station. These HIPR-based weights permit further refinement of our stacked waveforms. Our approach is detailed in Figure 3 and in the following subsections, and an example is provided in Supporting Information S1.

3.1. Event and Station Weights for High-Quality Waveforms

For a given event (j) and a given *phase* (P or PcP), we define the total time-shift applied to the waveform recorded by station i as ${\delta T_{phase}}^{i,j}$. We also define a reference station (*RS*), whose corresponding time-shift is ${\delta T_{phase}}^{RS,j}$. The interstation time-shift difference (DT) for event j and station i is defined as:

$$\mathrm{DT}_{phase}{}^{j}(i,RS) = {\delta T_{phase}}^{i,j} - {\delta T_{phase}}^{RS,j}. \tag{1}$$

The DT values allow us to examine how a given station behaves relative to any particular *RS*. For our analysis, we cycled through each of the 15 TAMNNET stations, allowing each to serve as the *RS* for the array. The DT values were determined for each *RS* possibility and for each event. Ultimately, for the 227 events in our interstation subset, 51,075 DT(i,*RS*) values were computed for each phase (P or PcP).

Then, for each *RS* possibility, we computed the average and standard deviation of DT ($\mu\mathrm{DT}_{phase}(i,RS)$ and $\sigma\mathrm{DT}_{phase}(i,RS)$, respectively) across all events (see Supporting Information S1). Thus, for each TAMNNET station, we have historical averages and standard deviations based on the differences in a given station's measurements with respect to those of all other stations across the full data set. The historical average at any *RS* (i.e., $\mu\mathrm{DT}_{phase}(i,RS)$) can be used to assess any particular measurement at the *RS*, for a given event. Specifically, for each *RS*, $\mu\mathrm{DT}_{phase}(i,RS)$ can be subtracted from $\mathrm{DT}_{phase}{}^{j}(i,RS)$ for each record to compute a difference from the average, which we define as:

$$\Delta\mathrm{DT}_{phase}{}^{i,j} = \mathrm{DT}_{phase}{}^{j}(i,RS) - \mu\mathrm{DT}_{phase}(i,RS). \tag{2}$$

The ΔDT differences document how any given differential measurement compares to the historical average for that *RS* and for station i. For a given *RS* and event j, we computed the L2 norm of the ΔDT values across all stations as (see Supporting Information S1):

$$\ell^2_{\Delta\mathrm{DT}phase} = \sqrt{\sum_i \left(\Delta\mathrm{DT}^{i,j}_{phase}\right)^2}. \tag{3}$$

We also determined the averages and standard deviations of these L2 norm values across all events for each *RS* ($\mu{\ell^2}_{\Delta\mathrm{DT}phase}$ and $\sigma{\ell^2}_{\Delta\mathrm{DT}phase}$; see Supporting Information S1). Computing $\mu{\ell^2}_{\Delta\mathrm{DT}phase}$ and $\sigma{\ell^2}_{\Delta\mathrm{DT}phase}$ from the historical interstation patterns allows assessment of the interstation time-shift differences for any specific event (and for the phase of interest). For example, if ${\ell^2}_{\Delta\mathrm{DTP}}$ is large compared to $\mu{\ell^2}_{\Delta\mathrm{DTP}}$ for a given event (and for a given *RS*), then the P-wave time shifts for that particular event are substantially different compared to the historical average of all other events, meaning it is less reliable and hence should receive a lower weight. We note that $\sigma{\ell^2}_{\Delta\mathrm{DT}phase}$ (for the given *RS*) helps to provide context on whether $\mu{\ell^2}_{\Delta\mathrm{DT}phase}$ is meaningful. We introduce event-specific weights (EVT_{phase}) to the data set based on $\mu{\ell^2}_{\Delta\mathrm{DT}phase}$ and $\sigma{\ell^2}_{\Delta\mathrm{DT}phase}$. After exploring various possibilities (see Supporting Information S1), we defined EVT_{phase} as:

$$\mathrm{EVT}_{phase} = \begin{cases} 1 & \text{if } \ell^2_{\Delta DTphase} < \left(\mu\ell^2_{\Delta DTphase} + 0.5\sigma\ell^2_{\Delta DTphase}\right) \\ 1 - \dfrac{\ell^2_{\Delta DTphase} - \left(\mu\ell^2_{\Delta DTphase} + 0.5\,\sigma\ell^2_{\Delta DTphase}\right)}{\mu\ell^2_{\Delta DTphase}} & \text{if } \ell^2_{\Delta DTphase} \geq \left(\mu\ell^2_{\Delta DTphase} + 0.5\,\sigma\ell^2_{\Delta DTphase}\right) \end{cases} \tag{4}$$

Figure 5a illustrates the range of EVT weights for both P and PcP across the 227 events in our high-quality interstation subset.

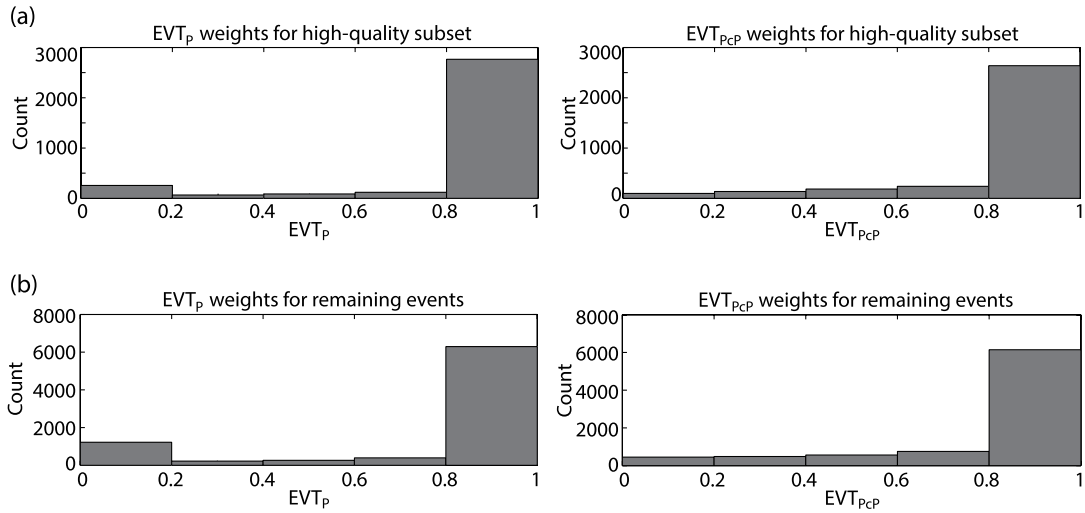

Figure 5. (a) Histograms showing the range of EVT_P and EVT_{PCP} weights for the events in our high-quality interstation subset (227 events total). 80% of the P data and 71% of the PcP data have full EVT weights of 1. (b) Same as (a) but now for the remaining events in our base data set (595 events total). 69% of the P data and 60% of the PcP data have full EVT weights of 1.

Our HIPR-based interstation time-shift differences have also been employed to determine associated station weights (STA) for the TAMNNET array. Specifically, for each *RS*, we computed the L2 norm of the $\sigma DT_P(i,RS)$ values defined above. That is:

$$\ell^2_{\sigma\mathrm{DTP}}(RS) = \sqrt{\sum_i (\sigma \mathrm{DT_P}(i,RS)^2)} \tag{5}$$

The $\ell^2_{\sigma\mathrm{DTP}}$ values provide a measure of stability (i.e., consistency) of the P-wave time shifts at each *RS*. That is, if $\ell^2_{\sigma\mathrm{DTP}}(RS)$ is small, it indicates that the P-wave interstation time shifts are consistent at that station and can be reliably used to assess the time shifts of individual events. Both the $\sigma\mathrm{DT_P}(i,RS)$ and $\ell^2_{\sigma\mathrm{DTP}}(RS)$ values are summarized in Supporting Information S1. The $\ell^2_{\sigma\mathrm{DTP}}$ values can be used to define $\mathrm{DT_P}$-based STA weights for each station in the array. To do so, the station with the smallest $\ell^2_{\sigma\mathrm{DTP}}$ is assigned a full weight of 1, while the station with the largest $\ell^2_{\sigma\mathrm{DTP}}$ is down-weighted by some user-specified percentage (DW%). The remaining stations are then weighted based on their fractional $\ell^2_{\sigma\mathrm{DTP}}$ relative to the minimum and maximum $\ell^2_{\sigma\mathrm{DTP}}$ values. That is,

$$\mathrm{STA} = 1 - \frac{\mathrm{DW\%}}{100}\left[\frac{\ell^2_{\sigma\mathrm{DTP}} - \min(\ell^2_{\sigma\mathrm{DTP}})}{\max(\ell^2_{\sigma\mathrm{DTP}}) - \min(\ell^2_{\sigma\mathrm{DTP}})}\right] \tag{6}$$

For the TAMNNET data set (Figure 6a; Supporting Information S1), station BEBP had the smallest $\ell^2_{\sigma\mathrm{DTP}}$ value (3.42), while station DONT had the largest value (7.61). Given this, station BEBP was assigned full weight (1), and station DONT was down-weighted by 30% (i.e., its STA weight from Equation 6 is 0.7). For the remaining TAMNNET stations, the corresponding STA weights were scaled using Equation 6, based on their fractional $\ell^2_{\sigma\mathrm{DTP}}$ relative to the minimum and maximum values at stations BEBP and DONT (Figure 6a; Supporting Information S1). We note that our STA weights are only based on the P waveforms given the higher SNR of P phases compared to PcP. From Figure 6a, one can see that there is a rough correlation between a TAMNNET station's STA and its distance from the coastline. Near-coastal stations, such as DONT and MICH, were located on a moving glacier and their corresponding signal quality was therefore somewhat lower, as reflected by their lower STA values. Stations located further inland were deployed on the more stable East Antarctic ice sheet and generally have higher STA values.

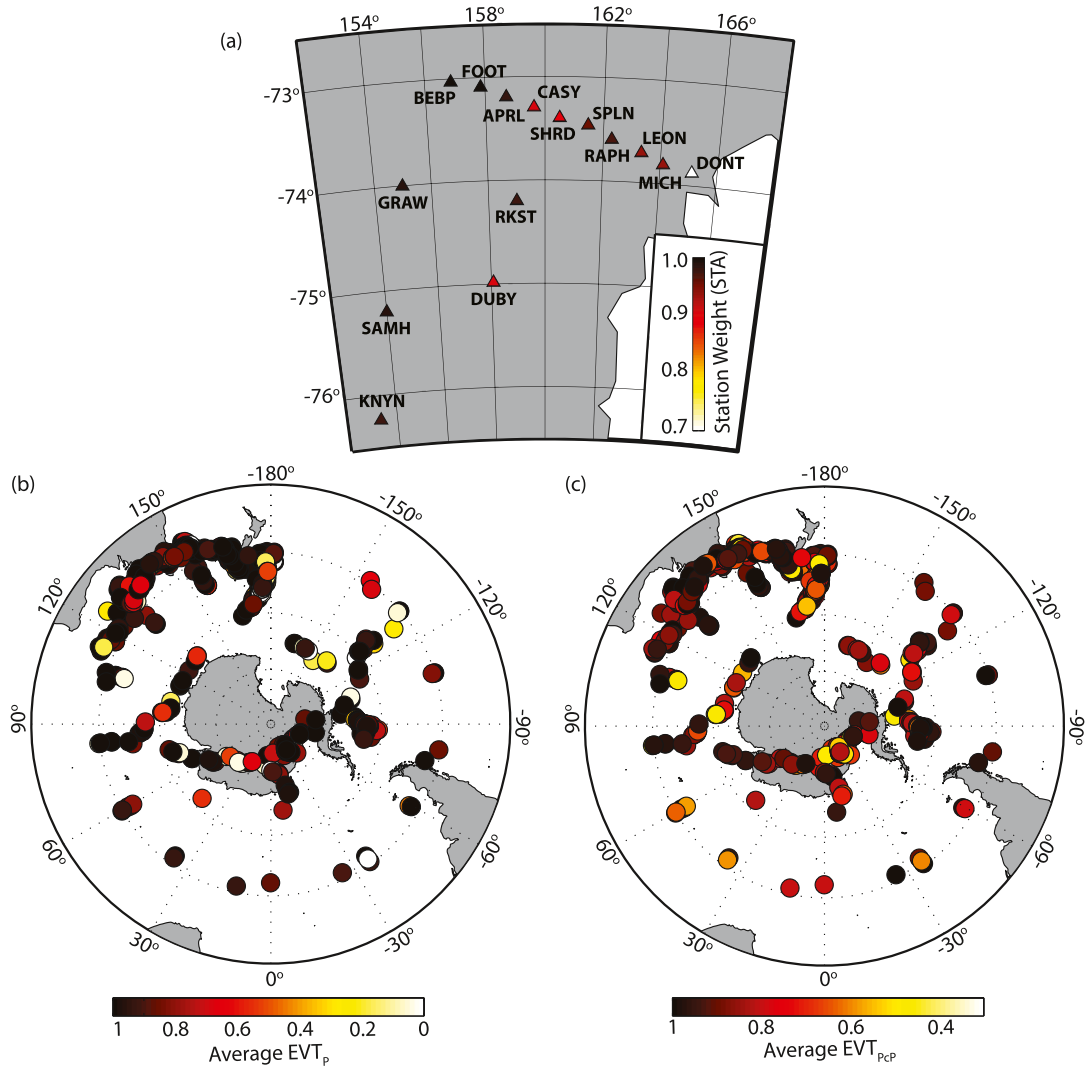

Figure 6. (a) TAMNNET stations (triangles) color-coded by their corresponding STA weights, as defined by Equation 6. (b) Average PcP CMB bounce point locations for all 822 events in our base data set, color-coded by their corresponding average EVT_P weight. (c) Same as (b) but now colors correspond to average EVT_{PcP} weights.

3.2. Event and Station Weights for Lower Quality Waveforms

The event weighting scheme described in Section 3.1 (Equation 4) was applied to the 227 events composing our high-quality data subset; however, we also wanted to apply this approach to the remaining 595 lower quality events in our base data set to assess if the HIPR method would allow us to improve their P and PcP stacks, thereby providing additional, reliable signals to assess ULVZ structure. Using the previously described relationship (Equation 1), DT values were computed for the remaining 595 events, allowing each TAMNNET station to have a turn as the *RS*, as before. However, the averages ($\mu DT_{phase}(i,RS)$) were not recomputed. Instead, we retained the average values that were determined using the 227 high-quality events (see Supporting Information S1), and these averages were used to compute $\Delta DT_{phase}^{\,i,j}$ as well as $\ell^2_{\Delta DTphase}$ for each event, as described in the previous section (see Equations 2 and 3). The $\ell^2_{\Delta DTphase}$ values were assessed using the $\mu\ell^2{}_{\Delta DTphase}$ and $\sigma\ell^2{}_{\Delta DTphase}$ terms, but similar to $\mu DT_{phase}(i,RS)$, these averages and standard deviations were again based on the high-quality event subset (see Supporting Information S1). Collectively, these values were used to compute EVT_{phase} for each record using the same weighting scheme described in Section 3.1 (Equation 4). Similar to Figures 5a, Figure 5b shows the range of EVT weights for both P and PcP, but now for the remaining 595 events that were not included in the high-quality interstation subset. Average EVT_P and EVT_{PcP} weights for all 822 events in our base data set are summarized in Figures 6b

and 6c, respectively. Unlike the STA weights (Figure 6a), there is no clear geographic patterns observed in the EVT_{phase} weights. We note that STA weights were not recomputed for the lower quality data set; instead, we retain those computed with the high-quality interstation subset (see Supporting Information S1).

4. Restacking Procedure

Of the 822 events in our base data set, 15 were removed because their corresponding EVT weights were 0. The removed events all had magnitudes <5.3 and had low SNR P arrivals. For the remaining 807 events, new P and PcP stacks were created by incorporating the interstation weights discussed in Section 3. As before (see Section 2), each P waveform was weighted by its CCC^2 value and SNR_{weight}; however, the waveforms were now also weighted by their corresponding EVT_P and STA weights. Collectively, these weights are used to define a final composite weight (FCW):

$$FCW_P = CCC^2 \times SNR_{weight} \times EVT_P \times STA \quad (7)$$

for each P record. For the PcP waveforms, a comparable weighting scheme was used, but we also applied the corresponding EVT_P weight to the PcP records. Specifically, for the PcP waveforms, the FCW is defined as:

$$FCW_{PcP} = CCC^2 \times SNR_{weight} \times EVT_P \times EVT_{PcP} \times STA \quad (8)$$

Taking this approach allows the higher SNR P waveforms to influence the weighting of the corresponding, lower SNR PcP records (and, conversely, if the P waveforms are poor quality, this approach further down-weights FCW_{PcP}). The iterative stacking approach outlined in Section 2 was again applied to both the P and PcP records to optimize the phase alignment and to update all event-representative stacks (Figure 3).

The newly updated stacks were then subjected to another round of visual inspection. Most of the 227 events composing our high-quality interstation subset have EVT weights with the maximum value of 1 (Figure 5a). While the applied STA weights modified the P and PcP stacks, the resulting waveforms for this subset were generally similar to those obtained with the original stacking procedure (see Event_2013.12.17.17.02.01.300 on Figure 7, for example). However, the HIPR weights lead to improved, higher SNR stacks for ~11% of the remaining lower quality events, as illustrated by the examples shown in Figure 7. This is significant because the applied approach has allowed us to retain events that would have been otherwise dismissed. For all data, the HIPR approach provides further confidence in the events chosen for later modeling and interpretation because the stacks are based on waveforms whose weights better reflect the station and event quality. Ultimately, 242 TAMNNET-recorded events, whose HIPR-weighted stacks show high SNR PcP signals, were retained for ULVZ assessment.

5. Additional Considerations

Since PcP phases travel greater distances through the Earth than direct P-waves, the PcP phases generally experience a higher degree of attenuative energy loss. Therefore, to make the stacks more comparable, the P-wave stacks must often be adjusted to account for the extra attenuation experienced by the PcP waves. We accomplish this by convolving each P-wave stack with a family of t* operators, ranging from 0.2 to 2.0. The t* operators represent the additional accumulated attenuation along the PcP ray path compared to P, where higher numbers correspond to greater attenuative energy loss (e.g., Bock & Clements, 1982; Hansen et al., 2020; Rost et al., 2005, 2010). For each event, the t*-convolved P-wave stacks were compared to the corresponding PcP stack, and the t* operator that produced an attenuated P response which most closely matched the PcP signal was selected. The optimal t* operator was determined using the CCC between the t*-convolved P and PcP stacks, but all comparisons were also visually inspected (see Supporting Information S1).

For some earthquakes, the radiation pattern can result in opposite polarities for the P and PcP phases; therefore, we also assessed the polarization of our stacks. 228 of our 242 events of interest have entries in the global centroid moment tensor (CMT) catalog (https://www.globalcmt.org; Dziewonski et al., 1981; Ekström et al., 2012), but we note that these CMTs are derived from long-period data. Therefore, the CMTs were used to predict event radiation patterns and thus the relative polarities of the examined high-frequency P and PcP data (Lin & Garnero, 2011). All radiation amplitude values were normalized between −1 and 1. If

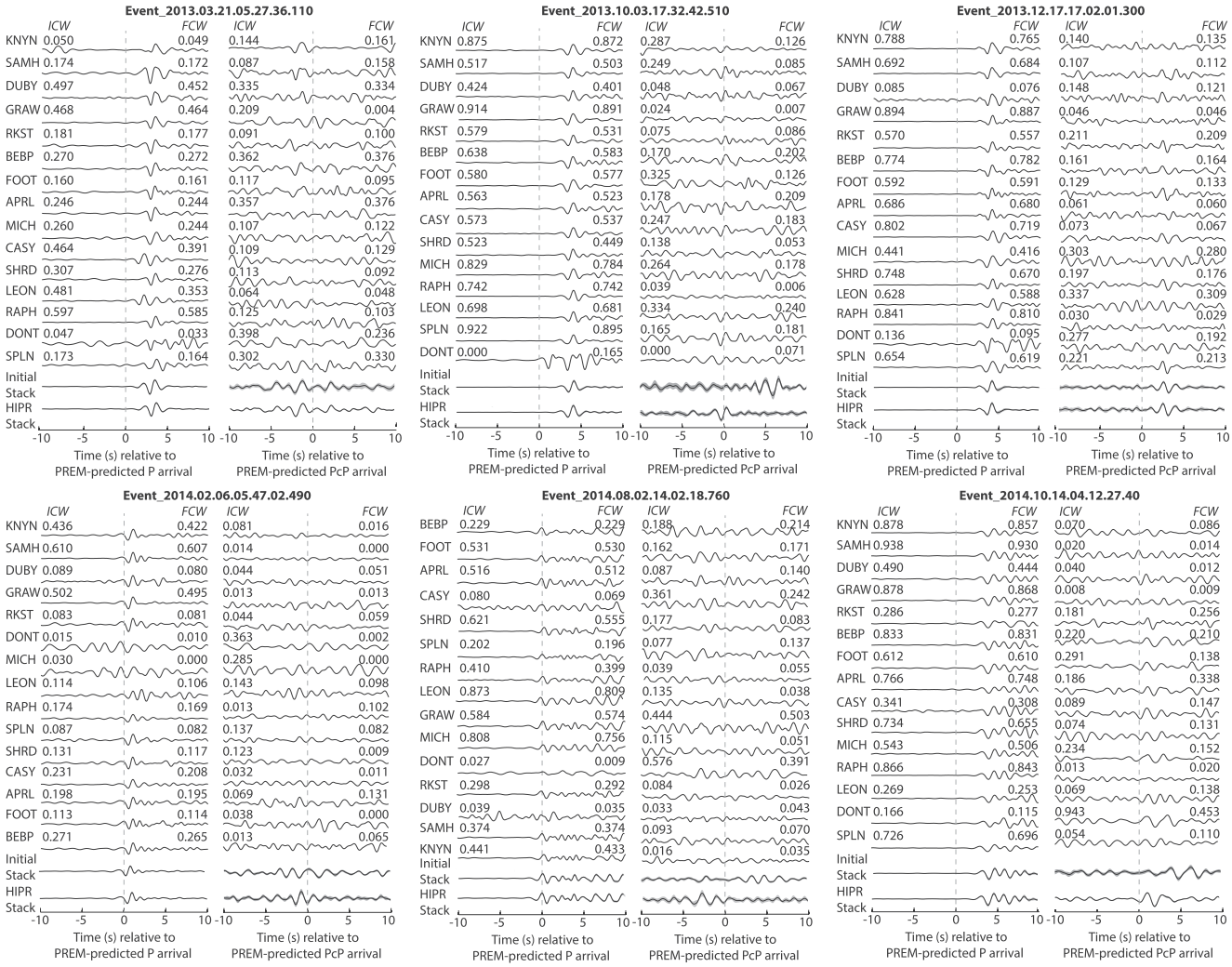

Figure 7. Illustration of HIPR-based stacking for six different example events. For each, the individual P and PcP waveforms are shown on the left and right panels, respectively, station names are listed on the left, and corresponding initial composite weights (ICW) and final composite weights (FCW) are listed above each trace. The waveform alignment corresponds to the interstation-based stacking procedure. Also shown are the P and PcP stacks obtained with the initial stacking procedure as well as with the HIPR-based stacking procedure. On all stacks, gray shading indicates one standard deviation of the stacked signal. Corresponding weights for each trace are summarized in Supporting Information S1. Event_2013.12.17.17.02.01.300 was included in our high-quality data subset, but all other events were part of the lower quality data set.

the predicted amplitudes for the P and PcP phases have opposite signs, a polarity change is likely given the take-off angle from the source. Further, if either the P or PcP predicted amplitudes are close to 0 (regardless of sign), one or both phases may be near the nodal plane, and a polarity reversal between phases is plausible. Otherwise, if both radiation amplitude values have the same sign and large values, the P and PcP phases should have the same polarity. For any event predicted to have a high likelihood of a polarity reversal (as well as for any event that was not in the global CMT catalog), we compared the t*-convolved P-wave stack to the corresponding PcP stack with both normal and reversed polarity (see Supporting Information S1). For these events, if the reversed polarity provided a better match between the P and PcP stacks, then that polarity was adopted. Of the 242 examined events, 20 had reversed polarity.

6. Example Application: Investigating ULVZ Structure Near New Zealand

To further illustrate the results provided by our new HIPR-based stacking approach, we highlight a group of events that sampled the lowermost mantle east of New Zealand (Figure 2b). This region was selected because it is the best sampled by the TAMNNET PcP data set and is of particular interest because it borders

the Pacific LLSVP. LLSVPs are large-scale mantle structures that extend hundreds of kilometers above the CMB and are characterized by negative δV_S of several percent relative to standard reference models (e.g., Cottaar & Lekic, 2016; Garnero et al., 2016). Some previous studies (e.g., Li et al., 2017; Zhao et al., 2017) have suggested that ULVZs may be preferentially concentrated near the boundaries of LLSVPs, associated with chemically distinct material advected there by mantle convection currents. Only three prior studies have investigated the CMB structure in the area east of New Zealand (Hansen et al., 2020; Thorne & Garnero, 2004; Thorne et al., 2020); therefore, our PcP results allow for further assessment of potential ULVZ-LLSVP relationships. Of our examined events, 90 probe the lower mantle structure in this region, and refined P and PcP stacks were generated for all of these earthquakes using our refined, HIPR-based stacking scheme.

6.1. Synthetic Modeling

Synthetic modeling was employed to assess the lowermost mantle structure sampled by our PcP waveforms. The generalized ray method (GRM, Gilbert & Helmberger, 1972) was used to compute a series of synthetic spike trains for the PcP and PdP phases as well as for three first-order reverberations generated within ULVZs (PcpdPcP, PcsdScP, and PdScsdScsP; Figure 1). The spike trains were calculated for the range of epicentral distances covered by our data and for a variety of ULVZ characteristics. Specifically, the ULVZ layer thickness was varied from 2 to 20 km in 2 km increments, $\delta\rho$ varied from −10% to 20% in 5% increments, δV_P varied from 0% to 20% in 1% increments, and δV_S varied from 0% to 50% in 2% increments. All $\delta\rho$, δV_P, and δV_S are relative to PREM (Dziewonski & Anderson, 1981). These ULVZ parameter ranges are similar to those typically found in previous investigations (e.g., see review by Yu & Garnero, 2018). A model without a ULVZ (i.e., the PREM model) was also included. Ultimately, for each epicentral distance, over 38,000 1-D synthetic models were generated.

For each event, a Hanning-tapered P-wavelet was extracted from the t*-convolved P stack using a ±3 s time-window centered on the P arrival. The wavelet was convolved with each of the GRM-generated synthetic spike trains to create a series of synthetic PcP waveforms ($\mathrm{PcP_{syn}}$), and the synthetic signals were correlated with the observed PcP stack ($\mathrm{PcP_{obs}}$), in order to align them at their point of maximum similarity and to determine their associated CCC. For the most extreme ULVZ models examined, the pre- and post-cursors arrive within ±8 s of the main phase (see Supporting Information S1). Therefore, $\mathrm{PcP_{obs}}$ and $\mathrm{PcP_{syn}}$ were compared over a 16 s window centered on the PcP arrival. The fit between $\mathrm{PcP_{obs}}$ and $\mathrm{PcP_{syn}}$ was assessed with a "Comparison Quality" (CQ) factor, defined as:

$$\mathrm{CQ} = \mathrm{CCC} \times \mathcal{G}, \tag{9}$$

where $\mathcal{G}$ is a measure of the goodness of fit between $\mathrm{PcP_{syn}}$ and $\mathrm{PcP_{obs}}$, defined by the sample-by-sample differences between their waveforms within the 16 s comparison window:

$$\mathcal{G} = 1 - \sqrt{\frac{\sum_{n=1}^{N}\left[\mathrm{PcP_{obs}} - \mathrm{PcP_{syn}}\right]^2}{\sum_{n=1}^{N}\left[\mathrm{PcP_{obs}}\right]^2}} \tag{10}$$

In Equation 10, N is the number of samples within the comparison window.

Two additional criteria were applied to ensure our interpretations are based on the most reliable results. First, we required that $\mathrm{PcP_{obs}}$ have SNR ≥ 1.5. Second, for the top 100 best-fit models, we require that their average CQ must be >0.2. These criteria help to ensure that the PcP signal is stable and that there is a good match between $\mathrm{PcP_{obs}}$ and $\mathrm{PcP_{syn}}$. For events meeting these criteria, we also determined the percent CQ improvement for each $\mathrm{PcP_{syn}}$ compared to that computed for the PREM synthetic to determine whether a ULVZ model fits the data significantly better than a non-ULVZ model. Here we specify that robust ULVZ evidence for any event requires the average CQ of the top 100 best-fit synthetic models to be at least 10% greater than the CQ of PREM. Otherwise, the synthetic modeling does not reliably distinguish between a CMB region possessing or lacking ULVZ structure. We note that our final HIPR-based P and PcP stacks and modeling results for the east New Zealand data set are openly available (see Acknowledgments).

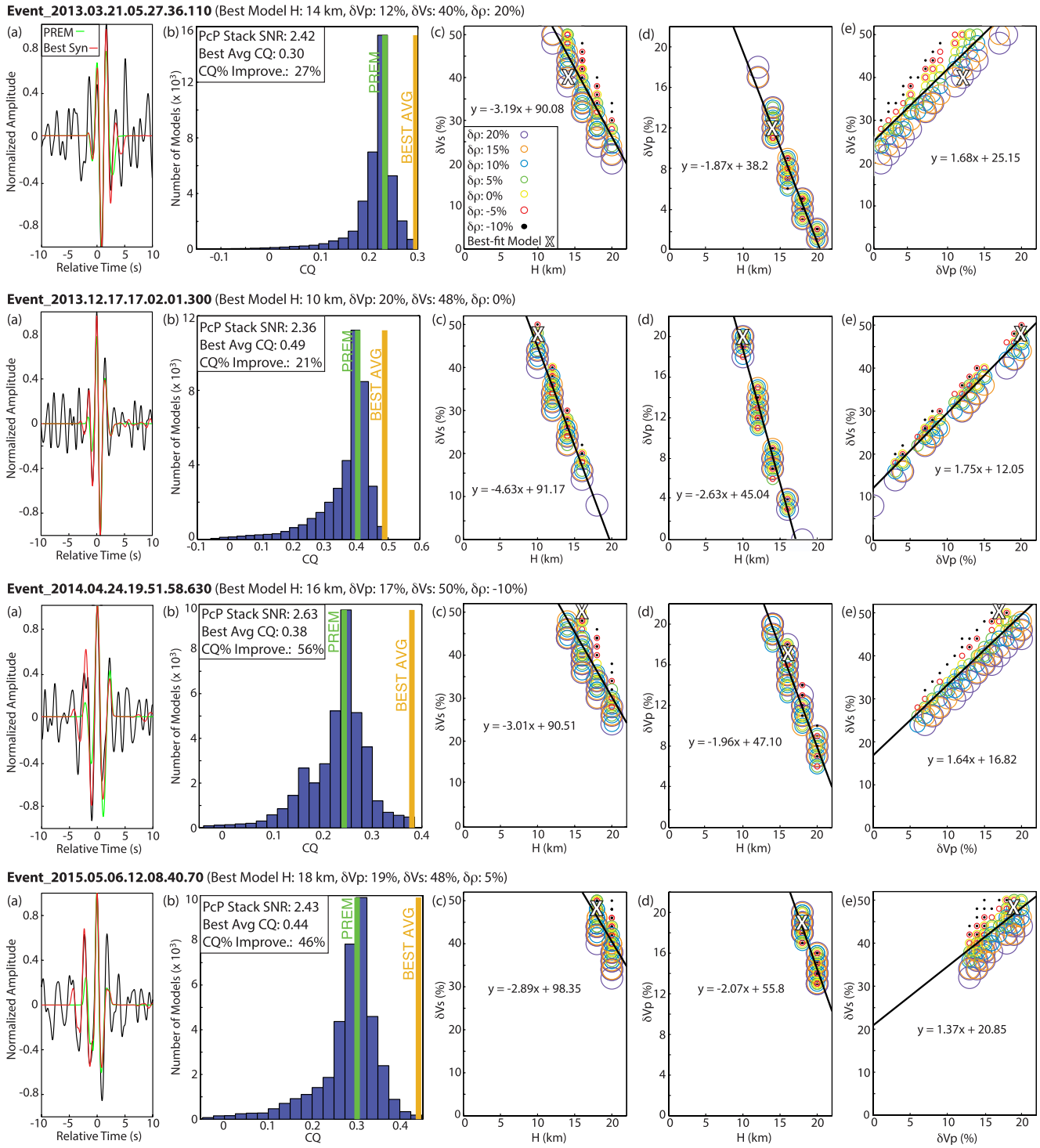

Figure 8. Synthetic modeling examples. For each event, (a) shows the HIPR-based PcP stack (black) along with the synthetics from the best-fit model (red) and from PREM (green). The ULVZ parameters for the best-fit model are listed next to the event ID (H: ULVZ thickness). (b) Histograms showing the range of CQ values across all synthetic models. The CQ values for PREM and the average CQ over the top 100 best-fit models are marked by green and orange lines, respectively. For reference, the PcP stack SNR, the average CQ value, and the average percent CQ improvement over PREM are listed on the upper left (note: averages are again over the top 100 best-fit models). (c–e) Scatter plots illustrating the range of ULVZ parameters for the top 100 best-fit models, with corresponding linear fits. Symbol colors represent different $\delta\rho$ values, as noted in the legend in the top row. The symbols are sized so that they can be nested since models that only differ by $\delta\rho$ will plot atop one another. For reference, the parameters for the best-fit model (a) are indicated by the X on each scatter plot.

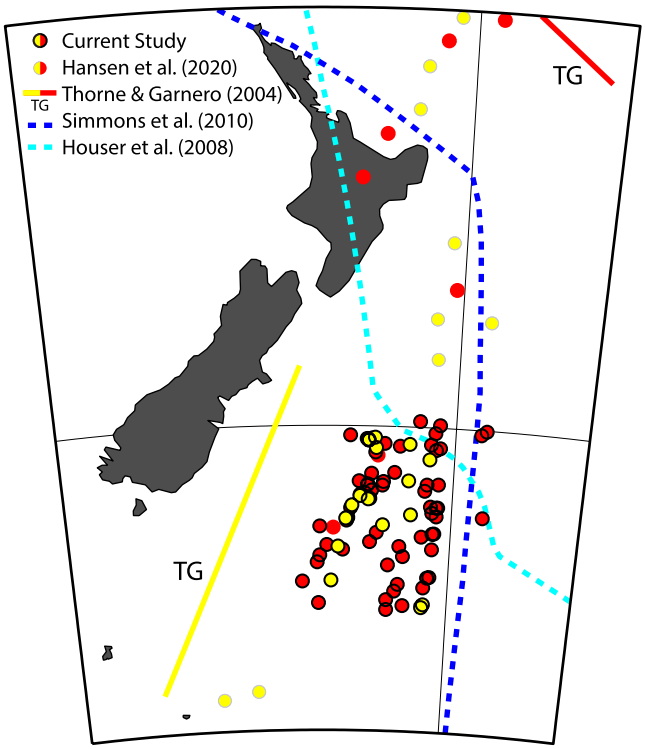

Figure 9. ULVZ comparisons between different studies in the vicinity of New Zealand (see green polygon on Figure 2b). Similar to the review by Yu and Garnero (2018), red markers indicate areas where ULVZ evidence has been found, and yellow markers indicate where ULVZ evidence is uncertain. PcP results from the current study are indicated by dots with bold black outlines, which are plotted at each event's average CMB bounce point. Remaining dots show ScP results from Hansen et al. (2020), and lines marked "TG" indicate results from the SP_dKS study by Thorne and Garnero (2004). Thorne et al. (2020) found no ULVZ evidence in this region. The dashed cyan and blue lines denote the boundary of the Pacific LLSVP as identified by Houser et al. (2008) and Simmons et al. (2010), respectively.

6.2. ULVZ Results

Six of the 90 New Zealand events did not meet the specified PcP_{obs} SNR criterion and an additional three events fell below the average CQ threshold; therefore, we focused our assessment on the remaining 81 events. Of these, 63 show robust ULVZ evidence as defined by the average percent CQ improvement threshold (10%). We note that ~15% of these events had PcP stacks that were improved by our HIPR-based weighting scheme and hence were retained for ULVZ assessment (see Section 4). The remaining 18 events fell below the specified percent CQ improvement threshold and hence provide uncertain ULVZ evidence (see Supporting Information S1). Examples of our modeling results are shown in Figure 8.

Modeling tradeoffs between ULVZ thickness and velocity reduction are common (e.g., Cottaar & Romanowicz, 2012; Garnero & Helmberger, 1998; Rost et al., 2005; Thorne et al., 2013; To et al., 2011). That is, a model with a thicker ULVZ and a smaller velocity reduction may fit the data equally well as a model with a thinner ULVZ and a larger velocity reduction. ~58% of our 81 modeled New Zealand events show such characteristic tradeoffs, as illustrated in the examples shown in Figure 8. However, this tradeoff is expected for fairly flat (at least locally) 1-D ULVZ structure; therefore, the lack of such linear tradeoffs for the remaining modeled events may reflect more complicated 3-D ULVZ structure (Hansen et al., 2020). If we focus on the top 100 best-fit models for each of the 63 events meeting our ULVZ criteria, the average ULVZ layer thickness (±1 standard deviation) across the study region is 16 ± 2 km, with average δV_P and δV_S of 13% ± 3% and 30% ± 7%, respectively, resulting in an average δV_S:δV_P of 2.3:1. If we instead only focus on the 47 events displaying linear tradeoffs in ULVZ characteristics, thereby potentially avoiding complex waveforms from 3-D ULVZ structure, the average slope of the δV_P versus δV_S plots indicates a δV_S:δV_P of 1.7:1. This is notable because previous studies that advocate for ULVZs being associated with partial melt along the CMB typically report higher δV_S:δV_P, averaging about 3:1 (e.g., Berryman, 2000; Garnero & Vidale, 1999; Reasoner & Revenaugh, 2000; Rost et al., 2006; Williams & Garnero, 1996; Yu & Garnero, 2018).

6.3. Comparison to Previous Studies and ULVZ Interpretation

Figure 9 shows a comparison of our PcP results in relation to previous investigations in our study area. As part of their global study, Thorne and Garnero (2004) examined the lowermost mantle structure both northeast of New Zealand as well as in a region just to the east of the south island (Figure 9). That investigation used SP_dKS waves, which can be difficult to interpret because of uncertainty on whether the imaged ULVZ structure is present along the source- versus receiver-side of the SP_dKS ray path (unless there is good crossing ray path coverage, e.g., Thorne et al., 2021). Thorne and Garnero (2004) find ULVZ evidence in the region northeast of New Zealand, with possible, though less certain, evidence along the CMB adjacent to the south island (Figure 9). Thorne et al. (2020) also examined SP_dKS waves in their global assessment of ULVZ structure, a small number of which sample the lowermost mantle east of New Zealand, but they did not find any evidence for ULVZ structure in this region. Hansen et al. (2020) modeled core-reflected ScP phases also recorded by TAMNNET. That study identified 10 events that displayed robust ULVZ evidence, with an additional 16 events showing possible but less certain evidence (Figure 9). There does not appear to be any compelling trend of where the robust versus uncertain ULVZs exist, but there is evidence for ULVZs throughout the general region. This is similar to the Idehara et al. (2007) study, who examined the lowermost mantle structure beneath the western and southern Pacific and found broad but irregular evidence for ULVZ structure.

The aforementioned studies as well as the PcP results from the current investigation all sample a portion of the CMB near the boundary of the Pacific LLSVP. Two different LLSVP margin locations from tomography studies by Houser et al. (2008) and Simmons et al. (2010) are shown in Figure 9 to illustrate that there is some uncertainty over where this boundary may be located, but we also note that the edges of the LLSVPs are, to first order, fairly consistent across all seismic tomography models (Cottaar & Lekic, 2016). Both our PcP results and those from prior studies (Figure 9; Hansen et al., 2020; Thorne & Garnero, 2004) indicate ULVZ structure along/near this boundary, which may suggest that the imaged ULVZs are associated with chemically distinct material moved by mantle convection currents. Geodynamic models show that compositionally unique ULVZs are driven toward the edges of LLSVPs (Hernlund & Tackley, 2007; Li et al., 2014, 2017; McNamara et al., 2010), and the approximately 2:1 δV_S:δV_P indicated by our PcP synthetics is more consistent with a compositional ULVZ origin as opposed to a solely thermal source (such as partial melting, e.g., Berryman, 2000; Williams & Garnero, 1996). Therefore, we interpret the ULVZ structure sampled by the TAMNNET data set as chemical heterogeneities (with or without partial melt) that have accumulated along the southwestern boundary of the Pacific LLSVP.

7. Conclusions

Our study presents a new iterative stacking routine that incorporates weighting based on interstation timing differences to improve signals of small-scale deep Earth structures. The method uses a HIPR approach, which permits any signal to be evaluated relative to expected interstation behaviors and thus weighted accordingly. The refined waveform stacks developed with our approach more objectively and systematically incorporate higher station and event quality, thereby providing further confidence in events chosen for synthetic modeling and interpretation. While not specifically aimed at identifying unclear seismic phases (below the noise level), the HIPR method does also allow some lower-quality events that may have been dismissed with more traditional stacking approaches to contribute to lower mantle and CMB investigations. To illustrate our method, we examined PcP phases recorded by the Antarctic TAMNNET array. The approach worked well for the examined network deployment duration and aperture, and while we have not tested the method on larger seismic arrays, we anticipate that HIPR would also be beneficial in these cases to establish relative time differences between stations, if sufficient historical event data is available. Results from our example application, which focus on a portion of the CMB east of New Zealand, provide strong evidence for ULVZ structure in this area, and we interpret the ULVZs as being associated with compositionally distinct material that has accumulated along the boundary of a LLSVP (Li et al., 2017).

Data Availability Statement

Data management handling was provided by the Incorporated Research Institutions for Seismology (IRIS) Data Management Center (DMC), and all TAMNNET data are openly available through the DMC (http://www.fdsn.org/networks/detail/ZJ_2012). Our final HIPR-based P and PcP stacks and all ULVZ modeling results are available at https://zenodo.org/deposit/4950169.

Acknowledgments
The authors would like to thank Mingming Li for his helpful discussions related to ULVZ-LLSVP relations and two anonymous reviewers as well as editor Michael Bostock for their thorough critiques of the manuscript. The IRIS DMC is funded through the Seismological Facilities for the Advancement of Geoscience (SAGE) award of the NSF under cooperative support agreement EAR-1851048. Funding for this research was provided by the NSF grants ANT-1139739 and PLR-1643551 as well as NSF-NERC collaborative grant NE/R012199/1. Some figures were generated with Generic Mapping Tools (Wessel et al., 2013).

References

Andrault, D., Pesce, G., Bouhifd, M. A., Bolfan-Casanova, N., Hénot, J.-M., & Mezouar, M. (2014). Melting of subducted basalt at the core-mantle boundary. *Science*, *344*, 892–895. https://doi.org/10.1126/science.1250466

Berryman, J. G. (2000). Seismic velocity decrement ratios for regions of partial melt in the lower mantle. *Geophysical Research Letters*, *27*, 421–424. https://doi.org/10.1029/1999GL008402

Bock, G., & Clements, J. R. (1982). Attenuation of short-period P, PcP, ScP, and pP waves in the Earth's mantle, *Journal of Geophysical Research*, *87*, 3905–3918. https://doi.org/10.1029/JB087iB05p03905

Cottaar, S., & Lekic, V. (2016). Morphology of seismically slow lower mantle structures. *Geophysical Journal International*, *207*, 1122–1136. https://doi.org/10.1093/gji/ggw324

Cottaar, S., & Romanowicz, B. (2012). An unusually large ULVZ at the base of the mantle near Hawaii. *Earth and Planetary Science Letters*, *355–356*, 213–222. https://doi.org/10.1016/j.epsl.2012.09.005

Dobson, D. P., & Brodholt, J. P. (2005). Subducted banded iron formations as a source of ultra-low velocity zones at the core-mantle boundary. *Nature*, *434*, 371–374. https://doi.org/10.1038/nature03430

Dziewonski, A. M., & Anderson, D. L. (1981). Preliminary reference Earth model. *Physics of the Earth and Planetary Interiors*, *25*, 297–356. https://doi.org/10.1016/0031-9201(81)90046-7

Dziewonski, A. M., Chou, T.-A., & Woodhouse, J. H. (1981). Determination of earthquake source parameters from waveform data for studies of global and regional seismicity. *Journal of Geophysical Research*, *86*, 2825–2852. https://doi.org/10.1029/JB086iB04p02825

Ekström, G., Nettles, M., & Dziewonski, A. M. (2012). The global CMT project 2004-2010: Centroid-moment tensors for 13,017 earthquakes. *Physics of the Earth and Planetary Interiors*, *200–201*, 1–9. https://doi.org/10.1016/j.pepi.2012.04.002

Fretwell, P., Pritchard, H. D., Vaughan, D. G., Bamber, J. L., Barrand, N. E., Bell, R., et al. (2013). Bedmap2: Improved ice bed, surface and thickness datasets for Antarctica. *The Cryosphere*, *7*, 375–393. https://doi.org/10.5194/tc-7-375-2013

Garnero, E. J. (2000). Heterogeneity of the lowermost mantle. *Annual Review of Earth and Planetary Sciences*, *28*, 509–537. https://doi.org/10.1146/annurev.earth.28.1.509

Garnero, E. J., & Helmberger, D. V. (1998). Further structural constraints and uncertainties of a thin laterally varying ultralow-velocity layer at the base of the mantle. *Journal of Geophysical Research*, *103*, 12495–12509. https://doi.org/10.1029/98JB00700

Garnero, E. J., McNamara, A. K., & Shim, S. (2016). Continent-sized anomalous zones with low seismic velocity at the base of Earth's mantle. *Nature Geoscience*, *9*, 481–489. https://doi.org/10.1038/ngeo2733

Garnero, E. J., & Vidale, J. E. (1999). ScP: A probe of ultralow velocity zones at the base of the mantle. *Geophysical Research Letters*, *26*, 377–380. https://doi.org/10.1029/1998GL900319

Gassner, A., Thomas, C., Kruger, F., & Weber, M. (2015). Probing the core-mantle boundary beneath Europe and Western Eurasia: A detailed study using PcP. *Physics of the Earth and Planetary Interiors*, *246*, 9–24. https://doi.org/10.1016/j.pepi.2015.06.007

Gilbert, F., & Helmberger, D. V. (1972). Generalized ray theory for a layered sphere. *Geophysical Journal of the Royal Astronomical Society*, *27*, 57–80. https://doi.org/10.1111/j.1365-246X.1972.tb02347.x

Hansen, S. E., Carson, S. E., Garnero, E. J., Rost, S., & Yu, S. (2020). Investigating ultra-low velocity zones in the southern hemisphere using an Antarctic dataset. *Earth and Planetary Science Letters*, *536*, 116142. https://doi.org/10.1016/j.epsl.2020.116142

Hansen, S. E., Reusch, A., Parker, T., Bloomquist, D., Carpenter, P., Graw, J. H., & Brenn, G. R. (2015). The Transantarctic Mountains Northern Network (TAMNNET): Deployment and performance of a seismic array in Antarctica. *Seismological Research Letters*, *86*, 1636–1644. https://doi.org/10.1785/0220150117

Hernlund, J. W., & Bonati, I. (2019). Modeling ultralow velocity zones as a thin chemically distinct dense layer at the core-mantle boundary. *Journal of Geophysical Research*, *124*, 7902–7917. https://doi.org/10.1029/2018JB017218

Hernlund, J. W., & Tackley, P. J. (2007). Some dynamical consequences of partial melting in Earth's deep mantle. *Physics of the Earth and Planetary Interiors*, *162*, 149–163. https://doi.org/10.1016/j.pepi.2007.04.005

Hirose, K., Fei, Y., Ma, Y., & Mao, H.-K. (1999). The fate of subducted basaltic crust in the Earth's lower mantle. *Nature*, *397*, 53–56. https://doi.org/10.1038/16225

Hirose, K., Takafuji, N., Sata, N., & Ohishi, Y. (2005). Phase transition and density of subducted MORB crust in the lower mantle. *Earth and Planetary Science Letters*, *237*, 239–251. https://doi.org/10.1016/j.epsl.2005.06.035

Houser, C., Masters, G., Shearer, P., & Laske, G. (2008). Shear and compressional velocity models of the mantle from cluster analysis of long-period waveforms. *Geophysical Journal International*, *174*, 196–212. https://doi.org/10.1111/j.1365-246X.2008.03763.x

Hutko, A. R., Lay, T., & Revenaugh, J. (2009). Localized double-array stacking analysis of PcP: D" and ULVZ structure beneath the Cocos plate, Mexico, central Pacific, and north Pacific. *Physics of the Earth and Planetary Interiors*, *173*, 60–74. https://doi.org/10.1016/j.pepi.2008.11.003

Idehara, K., Yamada, A., & Zhao, D. (2007). Seismological constraints on the ultralow velocity zones in the lowermost mantle from core-reflected waves. *Physics of the Earth and Planetary Interiors*, *165*, 25–46. https://doi.org/10.1016/j.pepi.2007.07.005

Jenkins, J., Mousavi, S., Li, Z., & Cottaar, S. (2021). A high-resolution map of Hawaiian ULVZ morphology from ScS phases, *Earth and Planetary Science Letters*, *563*. https://doi.org/10.1016/j.epsl.2021.116885

Knittle, E., & Jeanloz, R. (1991). Earth's core-mantle boundary – Results of experiments at high-pressures and temperatures. *Science*, *251*, 1438–1443. https://doi.org/10.1126/science.251.5000.1438

Kohler, M. D., Vidale, J. E., & Davis, P. M. (1997). Complex scattering within D" observed on the very dense Los Angeles Region Seismic Experiment Passive Array. *Geophysical Research Letters*, *24*, 1855–1858. https://doi.org/10.1029/97GL01823

Lai, H., & Garnero, E. J. (2019). Travel time and waveform measurements of global multibounce seismic waves using virtual station seismogram stacks. *Geochemistry, Geophysics, Geosystems*, *21*, e2019GC008679. https://doi.org/10.1029/2019GC008679

Li, M., McNamara, A. K., & Garnero, E. J. (2014). Chemical complexity of hotspots caused by cycling oceanic crust through mantle reservoirs. *Nature Geoscience*, *7*, 366–370. https://doi.org/10.1038/ngeo2120

Li, M., McNamara, A. K., Garnero, E. J., & Yu, S. (2017). Compositionally-distinct ultra-low velocity zones on Earth's core-mantle boundary. *Nature Communications*, *8*, 177. https://doi.org/10.1038/s41467-017-00219-x

Li, Y., Deschamps, F., & Tackley, J. P. (2016). Small post-perovskite patches at the base of the lower mantle primordial reservoirs: Insights from 2-D numerical modeling and implications for ULVZs. *Geophysical Research Letters*, *43*, 3215–3225. https://doi.org/10.1002/2016GL067803

Lin, P.-Y., & Garnero, E. J. (2011). Discovery using ducttape excessively (DUDE), with EarthScope data. *EarthScope National Meeting, Conference Abstract*.

Liu, J., Li, J., Hrubiak, R., & Smith, J. S. (2016). Origins of ultralow velocity zones through slab-derived metallic melt. *Proceedings of the National Academy of Sciences*, *113*, 5547–5551. https://doi.org/10.1073/pnas.1519540113

Mao, W. L., Mao, H. K., Sturhahn, W., Zhao, Z. Y., Prakapenka, V. B., Meng, Y., et al. (2006). Iron-rich post-perovskite and the origin of ultralow velocity zones. *Science*, *312*, 564–565. https://doi.org/10.1126/science.1123442

McNamara, A. K., Garnero, E. J., & Rost, S. (2010). Tracking deep mantle reservoirs with ultra-low velocity zones. *Earth and Planetary Science Letters*, *299*, 1–9. https://doi.org/10.1016/j.epsl.2010.07.042

Mori, J., & Helmberger, D. V. (1995). Localized boundary layer below the mid-Pacific velocity anomaly identified from a PcP precursor. *Journal of Geophysical Research*, *100*, 20359–20365. https://doi.org/10.1029/95JB02243

Persh, S. E., & Vidale, J. E. (2004). Reflection properties of the core-mantle boundary from global stacks of PcP and ScP. *Journal of Geophysical Research*, *109*(B4). https://doi.org/10.1029/2003JB002768

Rawlinson, N., & Kennett, B. L. N. (2004). Rapid estimation of relative and absolute delay times across a network by adaptive stacking. *Geophysical Journal International*, *157*, 332–340. https://doi.org/10.1111/j.1365-246X.2004.02188.x

Reasoner, C., & Revenaugh, J. (2000). ScP constraints on ultralow-velocity zone density and gradient thickness beneath the Pacific. *Journal of Geophysical Research*, *105*, 28173–28182. https://doi.org/10.1029/2000JB900331

Revenaugh, J., & Meyer, R. (1997). Seismic evidence of partial melt within a possibly ubiquitous low-velocity layer at the base of the mantle. *Science*, *277*, 670–673. https://doi.org/10.1126/science.277.5326.670

Rost, S., Garnero, E. J., Thorne, M. S., & Hutko, A. R. (2010). On the absence of an ultralow-velocity zone in the North Pacific. *Journal of Geophysical Research*, *115*(B4). https://doi.org/10.1029/2009JB006420

Rost, S., Garnero, E. J., & Williams, Q. (2006). Fine-scale ultralow velocity zone structure from high-frequency seismic array data. *Journal of Geophysical Research*, *111*(B9). https://doi.org/10.1029/2005JB004088

Rost, S., Garnero, E. J., Williams, Q., & Manga, M. (2005). Seismological constraints on a possible plume root at the core-mantle boundary. *Nature*, *435*, 666–669. https://doi.org/10.1038/nature03620

Simmons, N. A., Forte, A. M., Boschi, L., & Grand, S. P. (2010). GyPSuM: A joint tomographic model of mantle density and seismic wave speeds. *Journal of Geophysical Research*, *115*(B12). https://doi.org/10.1029/2010JB007631

Thorne, M. S., & Garnero, E. J. (2004). Inferences on ultralow-velocity zone structure from a global analysis of SPdKS waves. *Journal of Geophysical Research*, *109*(B8). https://doi.org/10.1029/2004JB003010

Thorne, M. S., Garnero, E. J., Jahnke, G., Igel, H., & McNamara, A. K. (2013). Mega ultra low velocity zone and mantle flow. *Earth and Planetary Science Letters*, *364*, 59–67. https://doi.org/10.1016/j.epsl.2012.12.034

Thorne, M. S., Leng, K., Pachhai, S., Rost, S., Wicks, J., & Nissen-Meyer, T. (2021). The most parsimonious ultralow-velocity zone distribution from highly anomalous SPdKS waveforms. *Geochemistry, Geophysics, Geosystems*, *22*, e2020GC009467. https://doi.org/10.1029/2020GC009467

Thorne, M. S., Pachhai, S., Leng, K., Wicks, J. K., & Nissen-Meyer, T. (2020). New candidate ultralow-velocity zone locations from highly anomalous SPdKS waveforms. *Minerals*, *10*, 211. https://doi.org/10.3390/min10030211

To, A., Fukao, Y., & Tsuboi, S. (2011). Evidence for a thick and localized ultra low shear velocity zone at the base of the mantle beneath the central Pacific. *Physics of the Earth and Planetary Interiors*, *184*, 119–113. https://doi.org/10.1016/j.pepi.2010.10.015

Wessel, P., Smith, W. H. F., Scharroo, R., Luis, J. F., & Wobbe, F. (2013). Generic mapping tools: Improve version released. *EOS Transactions AGU*, *94*, 409–410. https://doi.org/10.1002/2013eo450001

Wicks, J., Jackson, J., & Sturhahn, W. (2010). Very low sound velocities in iron-rich (Mg,Fe)O: Implications for the core-mantle boundary region. *Geophysical Research Letters*, *37*, 15. https://doi.org/10.1029/2010GL043689

Williams, Q., & Garnero, E. J. (1996). Seismic evidence for partial melt at the base of Earth's Mantle. *Science*, *273*, 1528–1530. https://doi.org/10.1126/science.273.5281.1528

Williams, Q., Revenaugh, J., & Garnero, E. J. (1998). A correlation between ultra-low basal velocities in the mantle and hot spots. *Science*, *281*, 546–549. https://doi.org/10.1126/science.281.5376.546

Yu, S., & Garnero, E. J. (2018). Ultralow velocity zone locations: A global assessment. *Geochemistry, Geophysics, Geosystems*, *19*, 396–414. https://doi.org/10.1002/2017GC007281

Zhao, C., Garnero, E. J., Li, M., McNamara, A., & Yu, S. (2017). Intermittent and lateral varying ULVZ structure at the northeastern margin of the Pacific LLSVP. *Journal of Geophysical Research*, *122*, 1198–1220. https://doi.org/10.1002/2016JB013449